Dual atmospheric windows infrared stealth research based on frequency selective surface

XU Cui-Lian[1], QU Shao-Bo[1*], WANG Jia-Fu[1], YAN Ming-Bao[1], PANG Yong-Qiang[2], WANG Wen-Jie[1], WANG Ai-Xia[1], FAN Qi[1]

(1. Department of Basic Science, Air Force Engineering University, Xi'an 710051, China；
2. School of Electronics and Information Engineering, Xi'an Jiaotong University, Xi'an, 710049, China)

Abstract：A novel and simple design of dual-stop-band frequency selective surface(FSS) for infrared stealth applications is proposed and investigated. The proposed structure consists of three layers, metallic four multiplexed cross resonators as the front layer, metal well-shaped structure as the bottom layer and a dielectric layer as the separator. The simulated results show that the proposed dual-stop-band FSS has high reflectivity in the two atmospheric windows (3.0～5.0 μm and 8.0～14.0 μm) for normal incidence waves, and the transmissvity is suppressed completely below 0.1. The influence of incident angle, period size and dielectric thickness on reflection and transmission were investigated. The proposed structure also shows good transmission stability in a large incident angle θ for both TE and TM modes at azimuthal angle $\varphi = 0°$. The stop-band principle of the proposed structure is formed not only by the electric resonance but also by the magnetic resonance.

Key words：infrared stealth, meta-material, frequency selective surface, infrared radiation

PACS：87. 50. W-, 44. 40. + a

基于频率选择表面的双大气窗口红外隐身研究

徐翠莲[1]， 屈绍波[1*]， 王甲富[1]， 闫明宝[1]， 庞永强[2]， 王雯洁[1]， 王爱霞[1]， 范 琦[1]
(1. 空军工程大学基础部 ,陕西 西安 710051；
2. 西安交通大学 电子信息工程学院 ,陕西 西安 710049)

摘要：为实现双大气窗口红外隐身,提出了一种新型双阻带频率选择表面(FSS). 该结构由三层材料组成:金属四个多路交叉十字型谐振器、金属井字型结构、中间由介质层隔开. 仿真结果表明,对于垂直入射波,所提出的双阻带 FSS 在两个大气窗(3.0～5.0 μm 和 8.0～14.0 μm)内具有较高的反射率,并且透射率被抑制到 0.1 以下. 研究了入射角、周期大小及介质厚度等对反射率和透射率的影响. 在 $\varphi = 0°$ 时,TE 和 TM 波在的宽入射角 θ 范围内均显示出良好的传输稳定性. 通过 FSS 在谐振频点的电场及表面电流的分析结果发现,3.0～5.0 μm 的反射是由于电谐振引起的而 8.0～14.0 μm 的高反射是由于电谐振与磁谐振共同引起的.

关 键 词：红外隐身;超材料;频率选择表面;红外辐射

中图分类号：TN21   **文献标识码**：A

Introduction

Low-emissivity infrared materials have been extensively studied due to their potential applications of infrared stealth techniques. Low-emissivity coatings are typically deposited on target for reducing the infrared radiation intensity. The main characteristic feature of low-emissivity coatings is high infrared reflectance. In the past decade, several kinds of low infrared emissivity materials such as core-shell composites, multilayer structures and nano-composite films have been developed[1-3]. High re-

flectance in the whole infrared band can significantly reduce the efficiency of electromagnetic waves transmission, but it will result in a rapid rise of temperature especially for targets of high-temperature components. It means that high temperature should be avoided in infrared stealth. However, conventional materials generally do not have frequency-selective characteristics. Since the atmosphere can absorb some electromagnetic wave of the infrared band and the infrared detecting instruments have to work in the atmospheric transparency windows with wavelength ranges of $3.0 \sim 5.0$ μm and $8.0 \sim 14.0$ μm, the expectation of controllable electromagnetic waves radiation has been a hot research topic for many years.

The spectral radiation signature, such as absorption, reflection, and transmission, could be modulated by patterning the surface with conducting or dielectric sub-wavelength elements. Spectral modifications have been readily shown in the literature for millimeter wave and infrared spectral regions and are well-known as frequency selective surfaces (FSS). As a spatial filter, on the one hand, FSS can be designed to demonstrate band-pass, band-stop, low-pass, or high-pass behavior[4-5]. On the other hand, its frequency response is not only function of frequency, but also functions of incident angle and polarization of the incoming electromagnetic wave. With growing interests in infrared (IR) stealth, remote sensing, IR detection applications, several FSS designs have been fabricated and tested. J A Bossard[7] investigated dual band metallo-dielectric FSS and all-dielectric FSS, the all-dielectric FSS had dual stop-bands in the mid-IR at around 80 THz and 90 THz. M J Dicken[8] demonstrated frequency tunable capability by using a near-infrared FSS based on VO_2 phase transition principle. They proposed a sandwiched VO_2 active layer between an Ag split ring resonators (SRRs) and sapphire substrate, which could realize ~ 100 nm wavelength modulation. Xiaotao Liang[9] utilized the properties of aligned nematic liquid crystal (LC) cells in the design of FSS. Metallo-dielectric FSS and an all-dielectric FSS were optimized to have a narrow stop-band in the mid-IR that could be tuned over a wide range of frequencies by an LC superstrate. However, conventional infrared FSSs are single layer structures, which results in narrow stop-band or pass-band. Zhixin Che and Changhui Tian[10] designed an IR FSS that composed of different size ring units. Consequently, the four different size rings show strong polarization sensitivity. In addition, the structure also has a narrow stop-band width of the long wavelength band of $8 \sim 14$ μm.

In this paper a dual-stop-band FSS for infrared stealth applications was proposed. The simulation results show that the proposed dual-stop-band FSS has high reflectivity in the two atmospheric windows ($3.0 \sim 5.0$ μm and $8.0 \sim 14.0$ μm) for normal incidence waves, and the transmissvity is suppressed completely under 0.1. In atmosphere absorption band of $5.5 \sim 7.6$ μm, the FSS exhibits high transmission. In addition, there is an absorption band in the $5.5 \sim 7.6$ μm which can passively cool themselves through transmit emission of heat to outer space. The structure is polarization independent.

1 Structure and design

The schematic of the designed dual-stop-band FSS is shown in Fig. 1. As shown in Fig. 1(a), metallic four multiplexed cross resonators consist of the top layer. The bottom layer is a metal well-shaped structure as shown in Fig. 1(b). The Fig. 1(c) shows the side structure of the unit that middle layer is dielectric. The unit cell has periodic dimensions of $p = 2.8$ μm in x-y plane, the width and the length of four crosses are $w = 0.2$ μm, $l = 1.3$ μm, the width of well-shaped structure is $w = 0.2$ μm. The employed metallic layer was the gold with Drude model for the dielectric function[11], $\varepsilon_m(\omega) = 1 - \omega_p^2/\omega(\omega + i\omega_c)$, Here the plasma frequency $\omega_p = 2\pi \times 2.175 \times 10^3$ THz, and the collision frequency $\omega_c = 2\pi \times 6.5$ THz. SiN_x layer is chosen as the dielectric spacer with dielectric constant 3.8 and loss tangent 0.025. The thicknesses of the gold cross resonators layer and SiN_x layer are $h_1 = 0.3$ μm and $h_2 = 1.4$ μm respectively. The thickness of gold well-shaped structure of the bottom is $h_3 = 0.1$ μm. The scattering parameters of the proposed structure are calculated from a commercial finite difference time domain (FDTD) method solver by CST Microwave Studio. The unit cell has periodic boundary conditions in x-y plane and open for z direction.
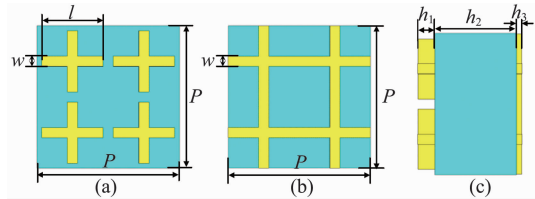

Fig. 1 The proposed FSS structure (a) Top view and, (b) Bottom view, (c) Side view
图 1 FSS 单元结构示意图(a)俯视图,(b)底视图,(c)侧视图

2 Simulation results and discussion

The reflection, transmission and absorption spectrum of the proposed FSS is shown in Fig. 2(a). The simulated results show that the proposed dual-stop-band frequency selective surface has high reflectivity in two atmospheric windows denoted as $3.0 \sim 5.0$ μm and $8.0 \sim 14.0$ μm for normal incidence wave, and the transmissivity completely less than 0.1. In the atmosphere absorption band of $5.5 \sim 7.6$ μm, there is a broad transmission band which leads to a high efficiency of electromagnetic wave transmission. It also can be seen from Fig. 2(a), in the atmosphere absorption band, there is an absorption band which leads to a high efficiency of heat radiation and good stealth for objects, according to Kirchhoff's law of thermal radiation. Fig. 2(b) shows the reflection of a single-lay FSS with cross structure, which has a high reflectance at 3-5 μm. As the thickness of the metal FSS screen increases, the reflectivity of 3-5

μm increases, but the steepness of the reflection curve decreases. Fig. 2(c) shows the reflectivity of a single-lay FSS with well-shaped structure, which has a high reflectance at 8-14 μm. The reflectance of 8 ~ 14 μm is lower than that of the dual-lays FSS. As the thickness of the well-shaped metal increases, the reflectance of 8 ~ 14 μm increases. Moreover, due to the symmetrical characteristic of the structure, it has almost the same response to transverse electric (TE) polarized light and transverse magnetic(TM) polarized light for normal incidence, the proposed FSS is nearly polarization independent.
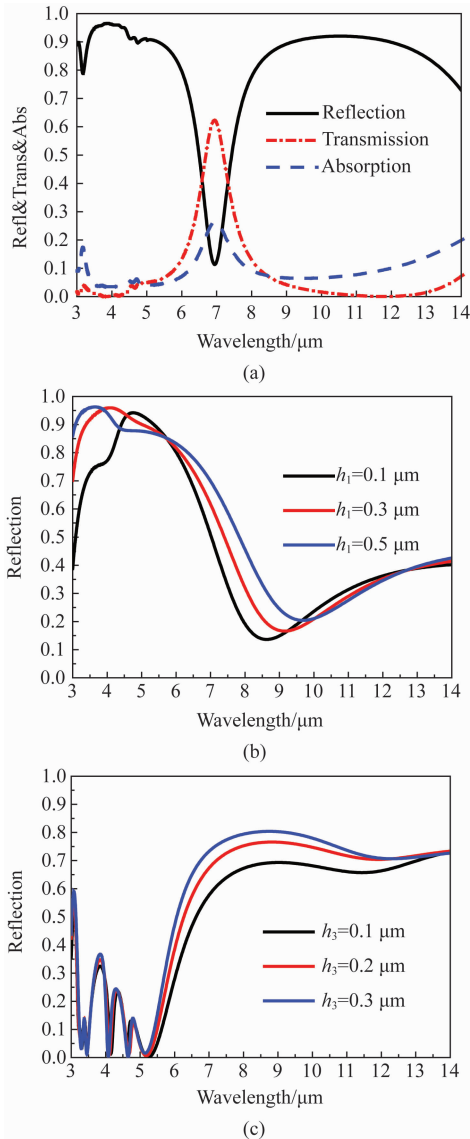

Fig. 2 (a) Simulated reflection, transmission and absorption spectrum of proposed FSS,(b) Reflection of single layer FSS with multiplexed cross resonators structures,(c) Reflection of single layer FSS with well-shaped structures
图 2 (a)双层 FSS 的反射率、透射率、吸收率曲线,(b)单层十字型 FSS 不同厚度的反射率,(c)单层金属井字型结构 FSS 不同厚度的反射率

We have further investigated the stability of transmission of incident angles θ varying from 0° to 80°. As shown in Fig. 3(a) and Fig. 3(b), the incident light are TE polarization and TM polarization at φ = 0°, respectively. For TE polarization, in the atmospheric absorption band of 5.5 ~ 7.6 μm, with the incident angle larger than 30°, the intensity of the transmission decreased quickly. However, in the atmospheric windows 3.0 ~ 5.0 μm and 8.0 ~ 14.0 μm, the spectral transmissivity is less than 0.1, the incident angle θ varies from 0° to 80°. For TM polarization, with incident angles θ varying from 0° to 80°, the transmission-band broadened in the atmospheric absorption window and the intensity of the transmission enhanced quickly.
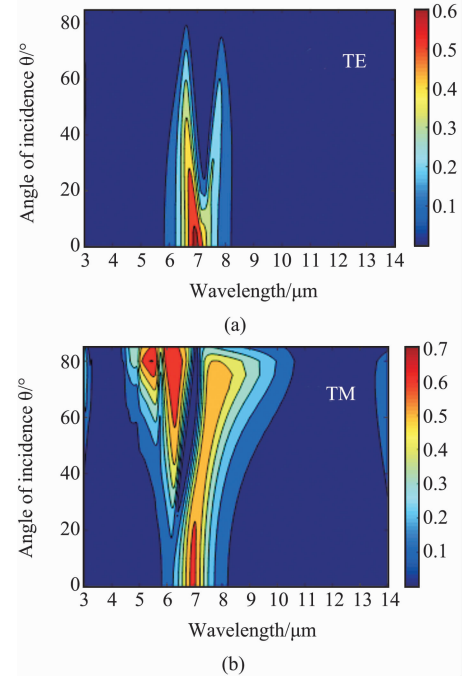

Fig. 3 The transmission as a function of incident angle for (a)TE and (b)TM polarization
图 3 FSS 不同入射角的透过率(a)TE 极化,(b)TM 极化

There are many parameters that affect FSS spectral behavior. Different structures of the conducting elements (or apertures) lead to various resonant characteristics. Also, FSS spectral performance is related to the distribution of the FSS elements and the electrical parameters of the surrounding media. The influence of these fundamental FSS parameters is discussed in the literature. The thickness of the gold well-shaped resonators layer is $h_3 = 0.1$ μm, keeping the other parameters unchanged and changing the thickness of the thickness h_1, as shown in Fig. 4(a), the value of h_1 increases, the transmittance of 3-5 μm decreases, and the peak of the transmission curve shifts toward to the long wavelength. Similarly, keeping the other parameters fixed, the thickness of the gold crossed resonators layer is setting $h_1 = 0.3$ μm. As shown in Fig. 4(b), the value of h_1 increases, the width of the transmission peak becomes narrower, and the peak of the transmission curve shifts toward to the short wavelength.

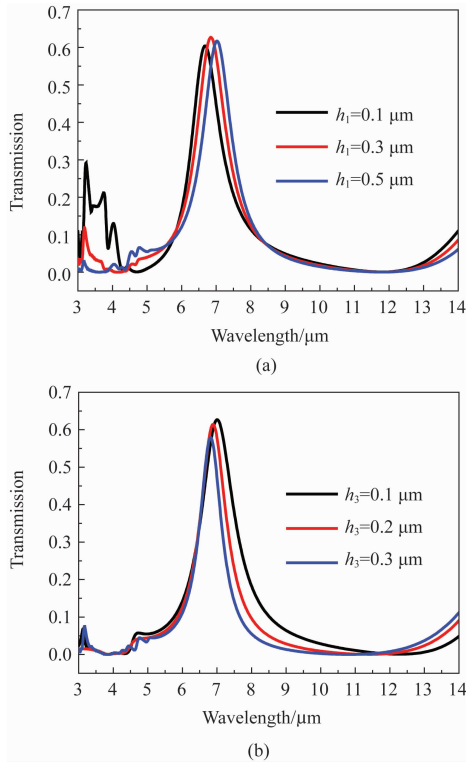Fig. 5(a) shows the reflection spectra for different

Fig. 4 (a) transmission spectra for different h_1, (b) transmission spectra for different h_3
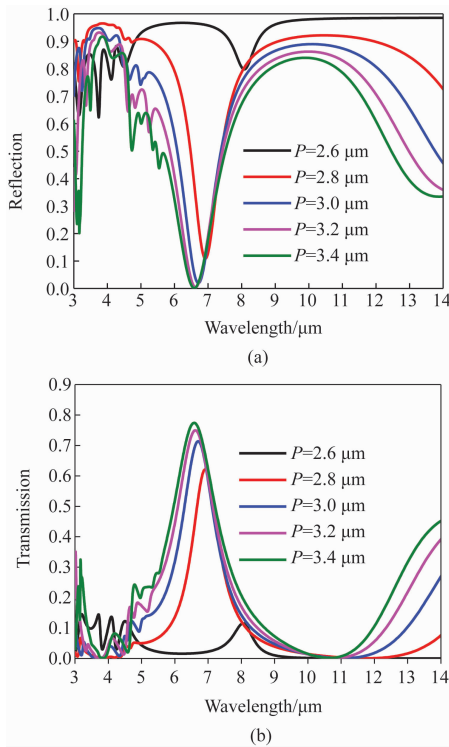图 4 (a)不同 h_1 对应的透射率曲线,(b) 不同 h_3 对应的透射率曲线

Fig. 5 (a) The refection and (b) transmission spectra for different periods
图 5 (a)不同周期对应的反射率曲线,(b)不同周期对应的透射率曲线

periods. It is apparent that the reflectivity in the two atmospheric windows (3.0~5.0 μm and 8.0~14.0 μm) decreases with the period increases. Fig. 5(b) shows the transmission spectra. It is apparent that the period has a great influence on the transmission maximum. It shows that the transmission maximum increases as period increases. At the same time, the width of transmission-stop-band decreases obviously. The peak wavelength of transmission experiences slight variation on small periods due to the coupling of adjacent gold crosses. As the period increases, the resonant wavelength is almost unchanged because the resonance condition does not change much. Only the gap between adjacent gold crosses increases, leading to the increase in transmission of the atmosphere absorption band of 5.5~7.6 μm. When the thickness h_2 of the thin SiN_x layer changes, as shown in Figs. 6(a) and 6(b), the resonant wavelength undergoes a red-shift while the transmission maximum almost over 56%. The shift of resonance is related to the change of SPPs wave vector for altering the dielectric environment[12].
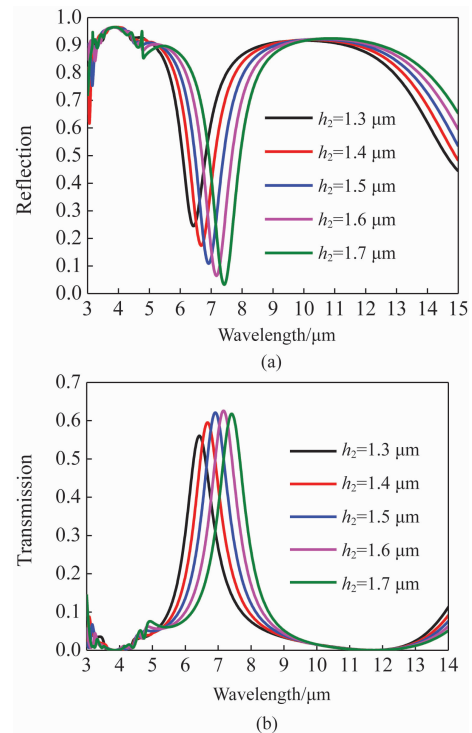

Fig. 6 (a) The refection and (b) transmission spectra for different dielectric thicknesses
图 6 (a)不同介质厚度对应的反射率曲线;
(b)不同介质厚度对应的透射率曲线

To better understand the principle of the resonant behavior, we monitored the surface current distributions of $λ = 3.8$ μm, and 12 μm for the TE polarized incident wave. The results are illustrated with Fig. 7 and Fig. 8. It can be seen from Fig. 7(a), at $λ = 3.8$ μm, the current intensity of the top cross resonators are larger than that of the bottom well-shaped structure. The current is mainly concentrated on the top surface, so the resonance of FSS of $λ = 3.8$ μm is mainly caused by the resonance

of the top layer cross unit. Fig. 7(b) shows the distributions of z-component electric field (real (Ez)) of cross resonators. It also can be seen from Fig. 7(b) that opposite charges accumulate at the edges of the four cross, which indicates the excitation of electric dipole resonance on the metal films.
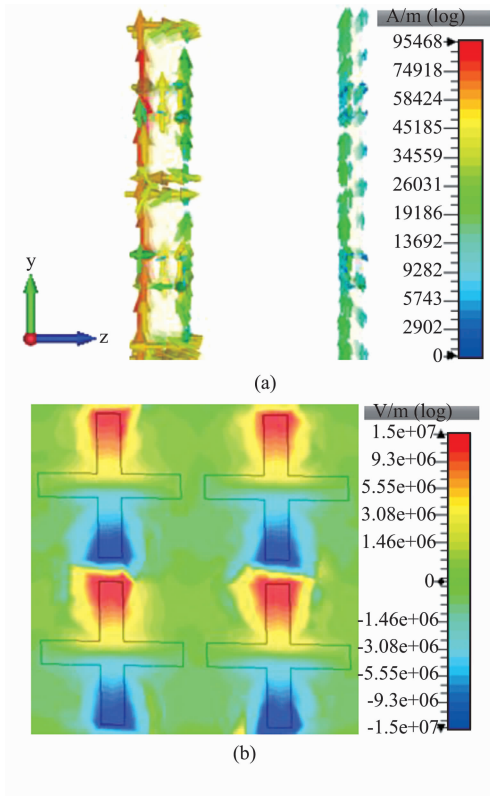

(a)

(b)

Fig. 7　(a) Side view of surface current distributions $\lambda = 3.8$ μm,(b) Distributions of z-component electric field (real (Ez)) of cross resonators
图 7　(a)波长 $\lambda = 3.8$ μm 处表面电流分布侧视图,(b) 十字型谐振器表面的电场 Z 分量

Fig. 8 shows the side view of surface current distributions of $\lambda = 12$ μm, the current is concentrated on the bottom of well-shaped structure, so the resonance for FSS of $\lambda = 12$ μm is mainly caused by the resonance of the bottom layer well-shaped structure. In addition, it can be seen that the two electric field loops with opposite orientations are formed into x-o-y plane at 12 μm. The surface currents on the metallic pattern and the metal groundsheet form current loops. Consequently, magnetic dipole is formed, which induce strong magnetic responses and cause strong enhancement of the magnetic field. Accordingly, strong magnetic resonances dominate the resonances. Therefore, the transmission-stop-band of proposed structure of $\lambda = 12$ μm is caused by not only the electric resonance of bottom layer well-shaped structure but also the magnetic resonance between cross unit and well-shaped unit.

In atmosphere absorption band of $5.5 \sim 7.6$ μm, the FSS exhibits an absorption band. In order to reveal the mechanism of the resonant absorption behavior, we monitored the surface current distributions of resonant
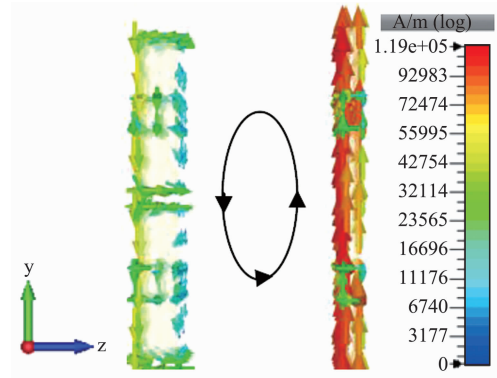

Fig. 8　Side view of surface current distributions $\lambda = 12$ μm
图 8　波长 $\lambda = 12$ μm 处表面电流分布侧视图

wavelength $\lambda = 5.8$ μm. As shown in Fig. 9, surface current distributed both the top and the bottom metal structures. Moreover, the metal cross and the metal well-shaped structure have the same current direction, so that the coupling between the metal structure caused the absorbing at 5.8 μm.
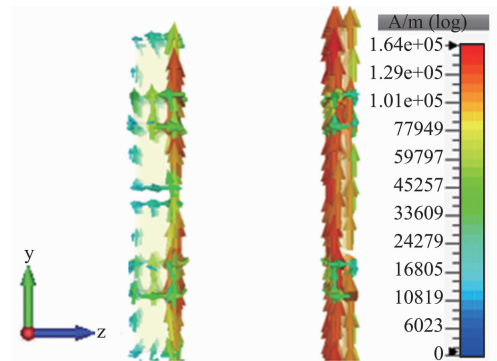

Fig. 9　Side view of surface current distributions $\lambda = 5.8$ μm
图 9　波长 $\lambda = 5.8$ μm 表面电流分布侧视图

3　Conclusions

In this paper, we proposed a new dual-stop-band FSS for infrared stealth applications. Our metamaterial structure is able to strongly suppress infrared radiation in two atmospheric windows of $3.0 \sim 5.0$ μm and $8.0 \sim 14.0$ μm, and the transmissivity is completely less than 0.1 for normal incidence wave. In the non-atmospheric window of 5.5-7.6 μm, there is a broad absorption-band and transmission-band which can passively cool themselves through radiative emission of heat to outer space. Moreover, due to the symmetrical characteristic of the structure, the intensity of transmission is stable varying with different azimuthal angles from 0° to 85°. The principle of the resonant the proposed structure is formed not only by the electric resonance but also by the magnetic resonance. The proposed structure shows promising potential application for the infrared stealth.

枯植物.尽管可以利用人工提取光谱特征实现研究对象的识别,但在特征选取的过程中,受研究人员个人因素的影响,往往无法保证识别结果的准确性和一致性.HOG 特征是图像处理领域中一种有效的对象识别描述符,不仅能表征光谱曲线局部形状的特点,也可以描述光谱曲线整体的内在特征.本文提出的基于 HOG 的方法与"总反射率"可以完整地描述光谱曲线.本研究对草原干枯植物与裸土的偏振光谱特征的研究有着重要意义,为干枯植物与裸土识别的研究提供了新的技术与方法.

References

［1］Diner D J, Xu F, Martonchik J V, *et al*. Exploration of a Polarized Surface Bidirectional Reflectance Model Using the Ground-Based Multiangle SpectroPolarimetric Imager ［J］. *Atmosphere*, 2012, **3**(4): 591 – 619.

［2］Zhang Y Q, Chen J M, Miller J R, *et al*. Leaf chlorophyll content retrieval from airborne hyperspectral remote sensing imagery ［J］. *Remote Sensing of Environment*, 2008, **112**(7):3234 – 3247.

［3］Landmann T, Piiroinen R, Makori D M, *et al*. Application of hyperspectral remote sensing for flower mapping in African savannas ［J］. *Remote Sensing of Environment*, 2015, **166**: 50 – 60.

［4］Gao J L, Meng B P, Liang T G, *et al*. Modeling alpine grassland forage phosphorus based on hyperspectral remote sensing and a multi-factor machine learning algorithm in the east of Tibetan Plateau, China ［J］. *ISPRS Journal of Photogrammetry and Remote Sensing*, 2019, **147**: 104 – 117.

［5］Comar A, Baret F, Viénot F, *et al*. Wheat Leaf Bidirectional Reflectance Measurements: Description and Quantifi-

cation of the Volume, Specular and Hot-spot Scattering Features ［J］. *Remote Sensing of Environment*, 2012, **121**(2): 26 – 35.

［6］Jiao Z T, Woodcock C, Schaaf C B, *et al*. Improving MODIS land cover classification by combining MODIS spectral and angular signatures in a Canadian boreal forest ［J］. *Canadian Journal of Remote Sensing*, 2011, **37**(2): 184 – 203.

［7］Roujean J L, Lacaze R. Global mapping of vegetation parameters from POLDER multiangular measurements for studies of surface-atmosphere interactions: A pragmatic method and its validation ［J］. *Journal of Geophysical Research Atmospheres*, 2002, **107**(D12): ACL6-1-ACL6-14.

［8］Chowdhary J, Cairns B, Waquet F, *et al*. Sensitivity of Multiangle, Multispectral Polarimetric Remote Sensing over Open Oceans to Water-leaving Radiance: Analyses of RSP Data Acquired during the MILAGRO Campaign ［J］. *Remote Sensing of Environment*, 2012, **118**(4): 284 – 308.

［9］Yang Han, Wen-Ru Xu, Lun Jin. A Study on the Polarized Reflectance Hyperspectral Characteristics and Models of Typical Saline Soil ［J］. *J. Infrared Millim. Waves*(韩阳, 徐文茹, 金伦. 典型盐渍化土壤偏振反射高光谱特征与模型分析. **红外与毫米波学报**), 2015, **34**(5): 606 – 612.

［10］Gu X, Cheng T, Xie D, *et al*. Analysis of surface and aerosol polarized reflectance for aerosol retrievals from polarized remote sensing in PRD urban region ［J］. *Atmospheric Environment*, 2011, **45**(36): 6607 – 6612.

［11］Sun Z Q, Peng Z Y, Wu D, *et al*. Photopolarimetric Properties of Leaf and Vegetation Covers over a Wide Range of Measurement Directions ［J］. *Journal of Quantitative Spectroscopy & Radiative Transfer*, 2018, **206**: 273 – 285.

［12］Dalal N, Triggs B. Histograms of Oriented Gradients for Human Detection: Proceedings of the 2005 IEEE Computer Society Conference on Computer Vision and Pattern Recognition (CVPR 05), 2005 ［C］. Washington, DC, USA: IEEE Computer Society, 2005: 886 – 893.

References

［1］Loka C, Park K R, Lee K. $SiO_2/TiO_2/n$-Si/Ag(Cr) /TiO_2 thin films with super hydrophilicity and low emissivity［J］. *Japanese Journal of Applied Physics*, 2016,**55**(01): 1 – 7.

［2］Zhang W G, Xu G Y, Shi X, *et al*. Ultra-low infrared emissivity at the wavelength of 3-5μm from Ge/ZnS one-dimensional photonic crystal［J］. *Photonics and Nanostructures Fundamentals and Applications*, 2015, **14**:46 – 51.

［3］Fang S J, Wang W, Yu X L, *et al*. Preparation of ZnO: (Al, La)/ polyacrylonitrile (PAN) nonwovens with low infrared emissivity via electrospinning［J］. *Materials Letters*. 2015,**143**:120 – 123.

［4］Srikanth G, Jack E, Fred T, *et al*. Frequency-selective surface based band pass filter in the near-infrared region ［J］. *Microwave and optical technology letter*. 2004,**41**(4): 266 – 269.

［5］Vegesna S, Yan H Z, Bernussi A. Terahertz two-layer frequency selective surfaces with improved transmission characteristics［J］. *IEEE Sci. Technolo.*, 2012, **2**(4): 441 – 448.

［6］James G, David S, Peter K, *et al*. Polarized infrared emission using frequency selective surfaces［J］. *Opt. Exp.*,

2010,**18**(5): 4557 – 4563.

［7］Bossard J A, Werner D H, Mayer T S, *et al*. The design and fabrication of planar multiband metallodielectric frequency selective surfaces for infrared applications ［J］. *IEEE Transactions on Antennas & Propagation*, 2006,**54**(4):1265 – 1276.

［8］Matthew J D, Koray A, Imogen M P, *et al*. Frequency tunable near-infrared metamaterials based on VO_2 phase transition ［J］. *Opt. Exp.*, 2009, **17**(20):18330 – 18339.

［9］Bossard J A, Liang X T, Li L, *et al*. Tunable Frequency Selective Surfaces and Negative-Zero-Positive Index Metamaterials Basedon Liquid Crystals［J］. *IEEE Transaction on Antennas and Propagation*,2008, **56**(5):1308 – 1319.

［10］Che Zh X,Tian Ch H,? Wang B K,? *et al*. An Infrared Frequency Selective Surface with Dual Stop-band［J］. *Infrared Technology*,(车志新,田昌会,王斌科,等. 一种双阻带红外频率选择表面. **红外技术**) 2017,**39**(7):594 – 597.

［11］Ma W, Wen Y ZH, Yu X M. Broadband metamaterial absorber at midinfrared using multiplexed cross resonators ［J］. *Opt. Exp.*, 2013,**21**(25):30724 – 30730.

［12］Nikitin A, Guinea F, Martin-Moreno L. Resonant plasmonic effects in periodic graphene antidot arrays［J］. *Appl. Phys. Lett.*, 2012,**101**(15):151119.